Received 7 February 2022; revised 13 April 2022 and 27 April 2022; accepted 27 April 2022. Date of publication 29 April 2022; date of current version 2 August 2022. The review of this article was arranged by Editor L. Hutin.

*Digital Object Identifier 10.1109/JEDS.2022.3171217*

# Interplay Between Charge Trapping and Polarization Switching in BEOL-Compatible Bilayer Ferroelectric Tunnel Junctions

**R. FONTANINI [1] (Graduate Student Member, IEEE), J. BARBOT [2] (Graduate Student Member, IEEE), M. SEGATTO [1] (Graduate Student Member, IEEE), S. LANCASTER [3] (Member, IEEE), Q. DUONG [3], F. DRIUSSI [1] (Member, IEEE), L. GRENOUILLET [2] (Member, IEEE), L. TRIOZON [2] (Member, IEEE), J. COIGNUS [2] (Member, IEEE), T. MIKOLAJICK [3,4] (Senior Member, IEEE), S. SLESAZECK [3], AND D. ESSENI [1] (Fellow, IEEE)**

1 DPIA, Università degli Studi di Udine, 33100 Udine, Italy
2 CEA, LETI, Univ. Grenoble Alpes, 38000 Grenoble, France
3 NaMLab gGmbH, 01187 Dresden, Germany
4 TU Dresden - IHM, 01069 Dresden, Germany

CORRESPONDING AUTHOR: R. FONTANINI (e-mail: fontanini.riccardo@spes.uniud.it)

This work was supported by the European Union through the BeFerroSynaptic Project under Grant GA:871737.

**ABSTRACT** We here report a joint experimental and theoretical analysis of polarization switching in ferroelectric tunnel junctions. Our results show that the injection and trapping of charge into the ferroelectric-dielectric stack has a large influence on the polarization switching. Our results are relevant to the physical understanding and to the design of the devices, and for both memory and memristor applications.

**INDEX TERMS** Ferroelectric tunnel junction, FTJ, HZO, synaptic memristor, charge trapping, interfacial charge, polarization switching, neuromoprhic computing, artificial intelligence.

## I. INTRODUCTION

The rise of artificial intelligence has emphasized the need for hardware platforms specifically conceived for new computational paradigms, such as crossbar arrays for the multiply and accumulate operation in artificial deep neural networks, and hybrid memristive-CMOS circuits for spike-based neuromorphic computing [1]. In particular, a large interest is presently focused on memristors, which are devices capable of a non volatile, multi-level adjustment of the conductance level [2]. Ferroelectric based CMOS-compatible electron devices offer promising options for memories and memristors [3], [4], with device concepts including Ferroelectric Tunnelling Junctions (FTJs) [5]–[7], as well as ferroelectric FETs [8], [9].

Energy efficiency is a main target for neuromorphic computing and it is a major concern for all computational technologies [10], [11]. Thanks to the field driven polarization switching, Ferroelectric Tunnel Junctions (FTJs) can provide high impedance and low energy synaptic devices. A four level operation has been demonstrated in a Metal-Ferroelectric-Dielectric-Metal (MFIM) structure [5]. In ferroelectric-dielectric (FE-DE) systems, charge injection through the thin dielectric and charge trapping are expected to play a prominent role in the switching and stabilization of the polarization [12]. In fact, large interface charge densities have been reported both for FeFETs [13], [14] and MFIM capacitors [15], [16], albeit some quantitative aspects are still actively debated [17].

In this paper we present a joint effort based on experiments and comprehensive numerical modelling to investigate the role of polarization switching, charge trapping and depolarization effects in TiN/$HfZrO_4$/$Al_2O_3$/TiN CMOS compatible FTJs. Our results help in clarifying the physical operation of the devices and provide a sound basis for the device design.

This work is licensed under a Creative Commons Attribution 4.0 License. For more information, see https://creativecommons.org/licenses/by/4.0/

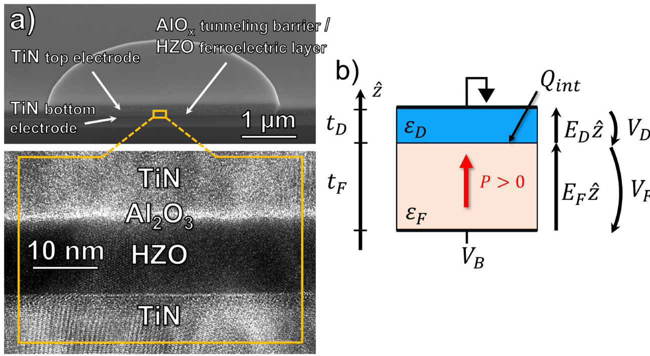


**FIGURE 1.** **a) High resolution TEM cross section of the TiN/1.5 nm $Al_2O_3$/10 nm HZO/TiN devices used in experiments; b) Sketch of the device template for numerical simulations.**

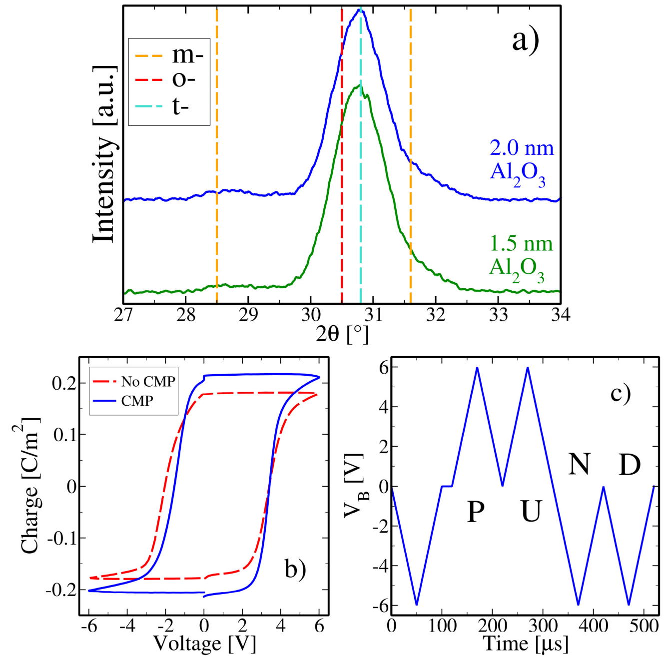


**FIGURE 2.** **a) 2$\theta$ scans taken in grazing-incidence geometry for films stacks with nominally 10 nm HSO and 1.5 nm $Al_2O_3$ (green) and 2 nm $Al_2O_3$ (blue). Dashed lines indicate the expected peak positions for the monoclinic (m-), polar orthorhombic (o-) and tetragonal (t-) phases; b) comparison of the switched charge measured on a 6 V - 10 kHz PUND waveform (represented in c), for samples with/without CMP bottom electrodes.**

## II. DEVICE FABRICATION AND MEASUREMENTS

Large area (7850 $\mu m^2$) FTJ structures were fabricated, featuring TiN top- and bottom-electrodes, an aluminium oxide ($Al_2O_3$) tunnelling layer at the top electrode interface and a 10 nm thick hafnium zirconium oxide ($Hf_{0.5}Zr_{0.5}O_2$ or, equivalently, $HfZrO_4$) ferroelectric between the bottom electrode and the tunnelling layer. The $Al_2O_3$ layer thickness was varied between 1.5 nm and 2.0 nm.

The TiN electrodes were deposited by physical vapor deposition at 350°C. Figure 1(a) reports a high resolution TEM cross section of the device. Prior to the HZO deposition, the TiN bottom electrode underwent chemical mechanical polishing (CMP) to improve roughness (rms= 0.1 nm). Both oxide layers were grown by atomic layer deposition at 280°C. $HfZrO_4$ films were deposited with HyALD and ZyALD precursors and $O_3$ as oxidant, at a rate of 0.8 Å/cycle using 1:1 supercycles of $HfO_2$ and $ZrO_2$ to ensure uniform stoichiometry. $Al_2O_3$ was deposited at a rate of 1 Å/cycle using TMA as a precursor and $O_3$ as oxidant. The maximum thermal budget for all structures was 450°C in order to be compatible with Back-End Of Line (BEOL) integration. Reactive Ion etching (RIE) was used to etch the TiN/$Al_2O_3$/$HfZrO_4$ stack with an etch stop in the TiN bottom electrode.

Grazing-incidence X-ray diffraction measurements were undertaken on nominally identical film stacks without CMP bottom electrodes, annealed at 500°C, on a Bruker D8 Discover X-ray analyzer. 2$\theta$ scans were measured in the grazing incidence geometry, at an incidence angle of 0.45°, to minimize the signal from the underlying substrate and allow the identification of crystal phases of the $HfZrO_4$ film. These data are plotted in Fig. 2(a) for stacks with 1.5 and 2 nm $Al_2O_3$, and the dashed lines indicate the expected peak positions of the strongest crystal reflections in these films [18]. The spectra were fitted with Gaussian peaks centred around these positions and the areas of the fitted peaks were used to calculate the phase fractions of the m-, o- and t-phases in our films.

Ferroelectricity in $HfZrO_4$ is attributed to the polar orthorhombic (o-) phase, while phase transformations can also occur during electric field cycling, contributing to the wake-up effect [19]. Thus the high o-phase fraction of these films in the pristine state (57% and 54% for 1.5 and 2 nm, respectively) suggests their good ferroelectric properties, despite the relatively thick dielectric interlayers. At the annealing temperatures used for both BEOL and reference samples, the $Al_2O_3$ layer remains amorphous.

This paper compares simulations with measurements obtained with the "Positive-Up-Negative-Down" (PUND) technique, that was originally conceived for Metal-Ferroelectric-Metal systems [20], [21], and is nowadays also routinely employed in MFIM device structures [22], [23], [24], [25]. The PUND method consists of a series of triangular pulses (see also Fig. 2(c)) and it is widely used in the characterization of ferroelectric devices [20]. In this work we used a 10kHz PUND with a delay time of 5ns between each pulse. Wake-up of the experimental results was achieved by bipolar triangular cycling (1000 cycles - 100kHz frequency) with a maximal voltage the same as the PUND.

Figure 2(b) represents the switched charge measured for 10 kHz triangular pulses of 6 V, for samples with (blue solid lines) and without (red dashed lines) CMP bottom electrodes. The bias was applied on the bottom electrode. The plotted curves are obtained by integrating the difference in P-U and N-D currents, which should provide an estimate of the switched polarization without influence of

**TABLE 1. Material parameters employed in simulations: $\varepsilon_r$ is the relative permittivity, and $\chi$, $\Phi_M$ are respectively the electron affinities of the dielectrics and the TiN workfunction. Calculations include domain to domain variations of $\alpha_i$, $\beta_i$, $\gamma_i$ parameters (with $i = 1, 2 \ldots n_D$), corresponding to a ratio $\sigma_{E_C}$ = 10% between the standard deviation and the mean value of the coercive field $E_C$. The resistivity for the ferroelectric is $\rho = 112\Omega m$ which is consistent with recently reported values for HZO based capacitors [32].**

| Material | Thick.[nm] | $\chi$[eV] | $\varepsilon_r$ [ad.] | $\Phi_M$ [eV] |
|---|---|---|---|---|
| $HfZrO_4$ | 10 | 2.4 | 34 | - |
| $Al_2O_3$ | 1.5, 2 | 1.4 | 10 | - |
| TiN | - | - | - | 4.55 |

leakage and displacement currents. It should be pointed out that this does not necessarily correspond entirely to the polarization switching current, as highlighted recently [26]. From Figure 2(b) it is clear, nonetheless, that the switched charge is larger for CMP devices. As the film stacks are nominally identical, the increase in switched charge may be related to an increased Pr due to different texturing of the TiN in the BEOL samples [27]. In addition, the reduced negative coercive voltage for the CMP process indicates a reduction in non-switching dead layers, and thus attests to the improvement of the bottom interface.

## III. MODELS AND COMPARISON TO EXPERIMENTS

The ferroelectric dynamics and electrostatics of an FTJ with the structure illustrated in Fig. 1(b) were self-consistently solved by using the multi-domain Landau, Ginzburg, Devonshire (LGD) model thoroughly described in [28]–[30]. The nominal values for the anisotropic constants used in simulations are $\alpha = -1.1 \cdot 10^8$ m/F, $\beta = -1.5 \cdot 10^{10}$ m$^5$/F/C$^2$, $\gamma = 1.85 \cdot 10^{11}$ m$^9$/F/C$^4$, which result in a remnant polarization $P_r \approx 24$ $\mu$C/cm$^2$ and coercive field $E_c \approx 1.8$ MV/cm, that are in fairly good agreement with polarization-voltage response of MFM samples deposited under similar conditions [31]. Our simulations typically include $n_D = 100$ domains, and we account for domain to domain random variations of $\alpha$, $\beta$, $\gamma$ (see Tab. 1). We have also verified that simulation results are practically insensitive to a further increase of the number of domains.

In our model the depolarization energy and fields are described by duly accounting for the three-dimensional nature of the electrostatics in the device. At each time $t$ and external bias $V_B(t)$, the LGD equations provide the domain polarization $P_i(t)$, the electric fields in the ferroelectric $E_{F,i}$ and in the dielectric $E_{D,i}$, and thus the band diagram in each domain (with $i = 1, 2 \ldots n_D$) [29].

As shown in Fig. 3, simulations neglecting any trapped charge at the FE-DE interface (or inside the dielectrics) result in much more stretched $P$-$V$ curves compared to experiments. These simulations are instead consistent experimental $P$-$V$ curves reported for an HZO capacitor serially connected to a discrete ceramic capacitor, which ensures a negligible charge injection through the dielectric [12], or to measurements in MFIM structures with thicker $Al_2O_3$ layers similarly suppressing charge injection [39]. These results

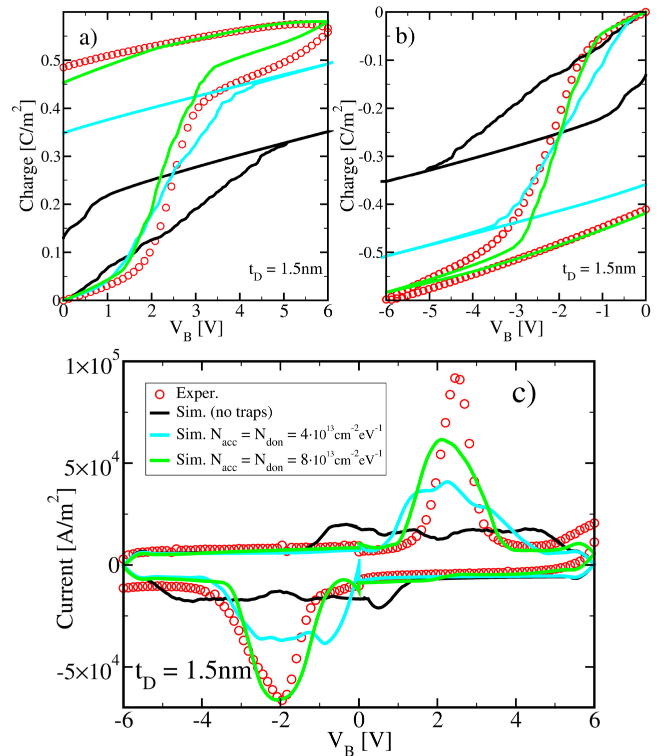


**FIGURE 3. Polarization versus voltage characteristics measured by the PUND method for a 50 $\mu$s width of the triangular pulse and for an $Al_2O_3$ FTJ with $t_D = 1.5$ nm. Results are reported for the P pulse (a), and for the N pulse (b). (c) Current versus voltage characteristics corresponding to the PUND measurements. Corresponding simulations are shown for no trapped charge (black solid line), and for different equivalent areal density of acceptor and donor type traps.**

are also qualitatively consistent with the analysis previously reported in [40].

Figure 3(c) illustrates the $I$-$V$ curves during the P and N pulses. In simulations with no traps (black solid line) the displacement current, $C_S(\partial V_B/\partial t)$, due to the linear polarization response is reproduced well (with $C_S = [1/C_D + 1/C_F]^{-1}$ and $C_D = \varepsilon_0\varepsilon_D/t_D$, $C_F = \varepsilon_0\varepsilon_F/t_F$). However the simulated switching current $(\partial P/\partial t)$ is spread over a large voltage range, which results in a relatively wide current plateau rather than a fairly narrow current peak exceeding the $C_S(\partial V_B/\partial t)$ contribution. This feature is again in stark disagreement with experiments.

The discrepancies between simulations and experiments in Fig. 3 suggest that charge injection and trapping in the dielectric stack plays an important role in the polarization switching for the FTJs, when considering the small dielectric thickness [12]. Hereafter we will assume that conduction in the $Al_2O_3$ layer is limited by tunnelling, even if transport mechanisms assisted by defects through Poole-Frenkel and hopping mechanisms are also possible in thin oxides [41]. We assume that the most important trapping effects for the polarization switching occur close to the FE-DE interface, and thus we describe the trap density and trapped charge in terms of areal densities. However, it is understood that

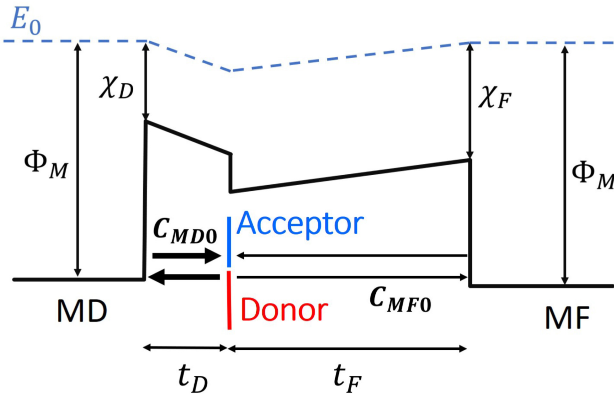


**FIGURE 4. Sketch of the band diagram in the TiN/HfZrO$_4$/Al$_2$O$_3$/TiN stack, showing also the energy position of acceptor and donor type traps. The capture rates $c_{MD0}$, $c_{MF0}$ are also illustrated as electron fluxes from the electrodes to the traps.**

these figures should be regarded as equivalent areal densities possibly summarizing also a charge trapping in the DE and FE films.

Acceptor and donor type traps at the FE-DE interface were described according to a first order dynamic equation. In particular, if we denote by $f_T$ the occupation of the trap at energy $E_T$ and with $c_{MD0}$, $c_{MF0}$ the capture rate from the metal MD and MF electrodes contacting respectively DE and FE (see Fig. 4), then $f_T$ is governed by the following equation:

$$\frac{\partial f_T}{\partial t} = c_{MD0}[f_{0,MD} - f_T] + c_{MF0}[f_{0,MF} - f_T], \quad (1)$$

where $f_{0,M}(E_T) = 1/[1 + \exp((E_T - E_{f,M})/(K_B T))]$ is the Fermi occupation function in the metal electrodes, with $E_{f,MF} = E_{f,MD} - qV_B$. In the derivation of Eq. (1) we used a detailed balance condition, ensuring that the steady state $f_T$ value at the equilibrium (i.e., for $V_B = 0$V) is given by the Fermi function. The capture rates can be expressed in terms of the tunnelling transmission between the FE-DE interface and each terminal MD or MF according to:

$$c_{M-0}(E_T) = \sigma_T \sigma_E \frac{m_\parallel}{2\pi^2 \hbar^3} \int_0^{+\infty} T_{M-}(E_T - \varepsilon) d\varepsilon, \quad (2)$$

where $\sigma_T$ [m$^2$], $\sigma_E$ [eV] are respectively an area and an energy cross section of the traps.

Equation (2) assumes an effective mass approximation in the metal electrodes[1] and an energy separability $E = E_\perp + \varepsilon(\mathbf{k})$, with the transverse energy $\varepsilon(\mathbf{k})$ being conserved in the tunnelling process [43]. The tunnelling transmission $T_{MD}(E_T - \varepsilon)$ and $T_{MF}(E_T - \varepsilon)$ were calculated through the WKB approximation, with the effective tunnelling masses $m_D$, $m_F$, and energy barriers $\Phi_D = (\Phi_{TiN} - \chi_D)$, $\Phi_F = (\Phi_{TiN} - \chi_F)$ in Tabs. 1 and 2. More details about the tunnelling model may be found in [44].

1. Here $m_\parallel$ corresponds to an effective mass for the density of states of the metals. In the absence of a better $m_\parallel$ determination, in calculations we used the popular assumption $m_\parallel \approx m_0$ [42].

**TABLE 2. Material parameters related to tunnelling and trapping in TiN/HfZrO$_4$/Al$_2$O$_3$/TiN FTJs. The value of $m_D$ for Al$_2$O$_3$ and $m_F$ for HZO are within the range reported in [33]–[35]; likewise the values for $\sigma_{T,acc}$ and $\sigma_{T,don}$ are within the admittedly quite wide range of values reported in the literature [36]–[38]. The energy cross-section $\sigma_E$ was set to 7 *meV* in all simulations. Acceptor and donor type traps are uniformly distributed in energy respectively from 0.6 to 2.6 *eV* and from 1.8 to 3.8 *eV* below the HZO conduction band, respectively (see also Fig. 4).**

| $t_D$ | $\sigma_{T,acc}$ [cm$^2$] | $\sigma_{T,don}$ | m$_D$ [m$_0$] | m$_F$ |
|---|---|---|---|---|
| 1.5 nm | $2.5 \cdot 10^{-16}$ | $10^{-16}$ | 0.2 | 0.4 |
| 2.0 nm | $5 \cdot 10^{-15}$ | $10^{-15}$ | 0.15 | 0.4 |

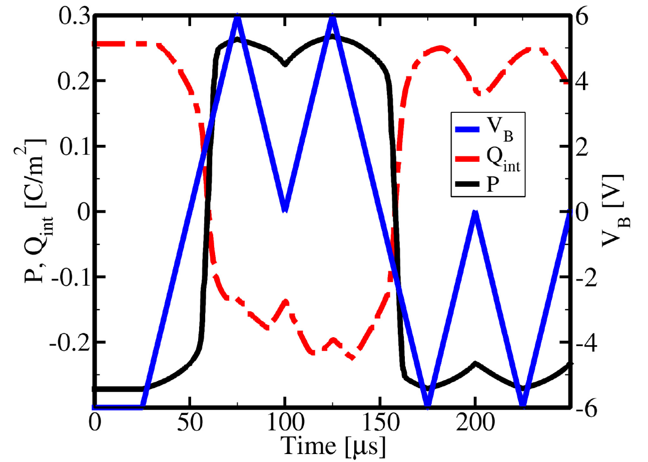


**FIGURE 5. Polarization, *P*, and interface charge, $Q_{int} = Q_{acc} + Q_{don}$, versus time during for the same PUND simulations as in Figs.3 (c). The Al$_2$O$_3$ thickness is $t_D$ = 1.5 nm and the trap densities are $N_{acc} = N_{don} = 8 \cdot 10^{13}$ 1/(cm$^2$eV). The $V_B$ waveform is also shown (blue line).**

The charges $Q_{acc}$, $Q_{don}$ trapped in acceptor and donor traps, respectively, can be written as:

$$Q_{acc} = \frac{-q}{n_D} \sum_{E_T} N_{acc} f_T(E_T) \Delta E, \quad (3a)$$

$$Q_{don} = \frac{q}{n_D} \sum_{E_T} N_{don} (1 - f_T(E_T)) \Delta E, \quad (3b)$$

where $N_{acc}$, $N_{don}$ denote the trap densities and $\Delta E$ is the energy step between the discrete trap levels. Equations (1) to (3a) refer to a single domain in the FTJ structure, and Eq. (1) was solved in all domains and self-consistently with the LGD equations for the ferroelectric dynamics.

Figure 3 suggests that simulations can be reconciled with experiments only by assuming a large equivalent trap density, and Fig. 3(c) shows that the corresponding simulated *I*-*V* plot can also track quite well the coercive voltage and the shape of the measured current. Figure 5 offers a simulation based insight about the behaviour of the average polarization and interface charge ($P$ and $Q_{int}$, both averaged over the device area) along a PUND waveform. In this example both positive and negative $P$ are compensated by $Q_{int}$ to a large extent. This is the basic mechanism by which the

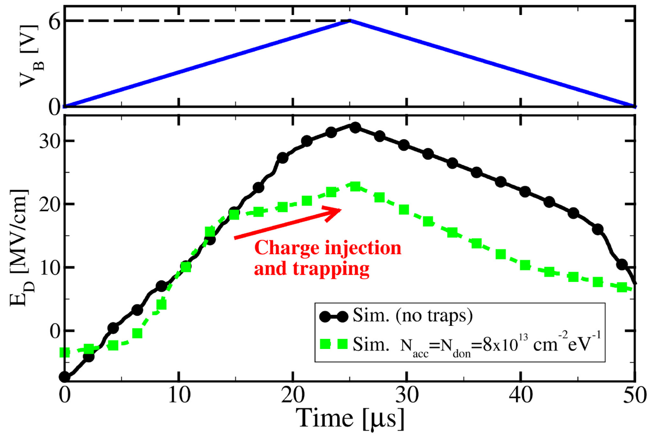


**FIGURE 6. Electric field across the $Al_2O_3$ layer during the P pulse analyzed in Fig. 3(a), hence for $t_D = 1.5$ nm.**

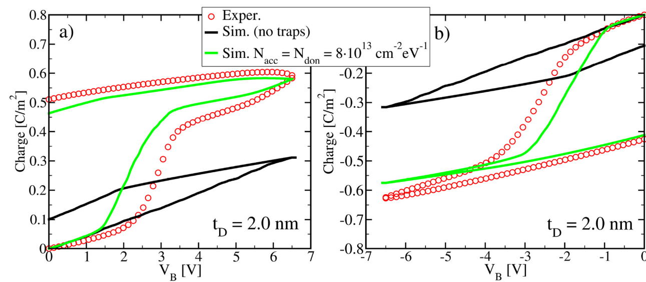


**FIGURE 7. Measured and simulated P-V curves for a PUND waveform as in Fig. 3, but for an $Al_2O_3$ FTJ with $t_D = 2.0$ nm.**

depolarization field can be reduced compared to the case with $Q_{int} \approx 0$ C/m$^2$, and the simulated *P-V* curves reconciled with experiments. Figure 6 also reports the simulated field, $E_D$, across the $Al_2O_3$ layer during the P pulse analyzed in Fig. 3(a). In simulations with no traps, $E_D$ exceeds 30 MV/cm at the $V_B$ peak, which is an unrealistically large value and would also lead to a huge tunnelling current. In the presence of traps, instead, when $E_D$ exceeds approximately 15 MV/cm electrons are injected through the dielectric and trapped at the FE-DE interface. The resulting building up of negative charge quenches the increase of $E_D$, which is a physical picture consistent with the one proposed in [12]. The reduction of $E_D$ induced by the trapped charge is accompanied by an increase of $E_F$, which is however much smaller in magnitude than $E_D$.

Figure 7 shows that the results are qualitatively similar for the FTJs having a slightly thicker $Al_2O_3$ layer. Even for $t_D = 2.0$ nm the simulations with no traps are in sharp disagreement with experiments. Moreover, the same trap densities result in a fairly good agreement with P-V and I-V curves for both $t_D = 1.5$ nm and 2.0 nm.

The experiments in Figs. 3 and 7 suggest that, if it is the charge injection through $Al_2O_3$ that feeds the charge trapping at the FE-DE interface, then such an injection must be similarly effective for $t_D = 1.5$ nm and 2.0 nm. To obtain this behaviour in our tunnelling based model, for the

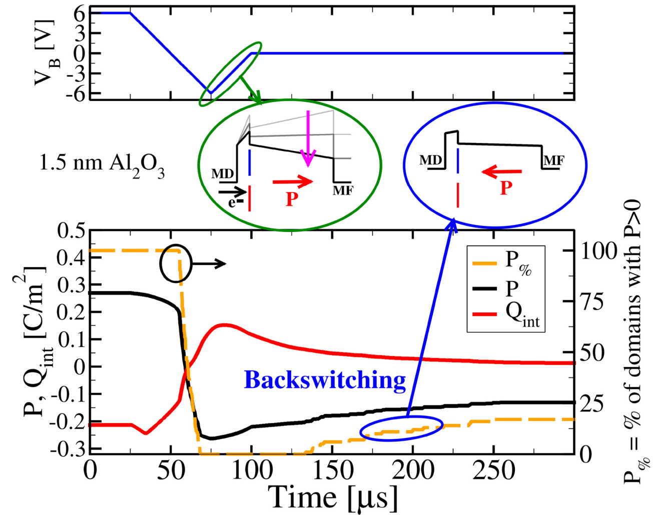


**FIGURE 8. Polarization (black line) and interface charge (red line) during an N pulse and the following retention phase at $V_B = 0$ V. The percentage of positive polarization domains (yellow dashed line, right $y$ axis) increases during the retention phase. Insets show the band diagram for negative (left) and a backswitched (right) polarization configurations.**

$t_D = 2.0$ nm case it was necessary to increase the trap cross section $\sigma_T$ and slightly decrease the $Al_2O_3$ tunnelling mass (see Tab. 2). The need for an empirical adjustment of these parameters may suggest that additional transport mechanisms are involved in $Al_2O_3$ [41].

## IV. IMPLICATIONS FOR FTJ DEVICE DYNAMICS

The results of the previous section suggest that charge injection and trapping play an important role in the polarization switching and stabilization in the MFIM-based FTJs at study. As a corollary, we found that the interface charge has implications for different aspects of the device design. Figure 8, for example, examines the polarization loss at $V_B = 0$ V after the N pulse of a PUND sequence, which is linked to detrapping. In the simulations of Fig. 8, in fact, a fraction of the donor traps that have positively charged during the N pulse lie below the Fermi level when $V_B$ goes back to zero. During the retention at $V_B = 0$ V such donor traps capture electrons and thus become neutral (see Eq. (1)). The resulting reduction of the positive interface charge $Q_{int} \approx Q_{don}$ enhances the depolarization field, which eventually leads to the back-switching of a fraction of domains.

Of course the behaviour in Fig. 8 is critically influenced by the position of the trap energy levels. However, a similar interplay between detrapping and back-switching is plausible in actual devices. As an example, the polarization loss along time was experimentally investigated in Fig. 9, where the delay between two consecutive, negative identical pulses was varied within nine orders of magnitude. The polarization loss was here defined as the ratio between the polarization switched during the S2 pulse divided by the counterpart during the S1 pulse. Figure 9 shows that the lost polarization increases with time from 100 ns to 10 ms and then saturates

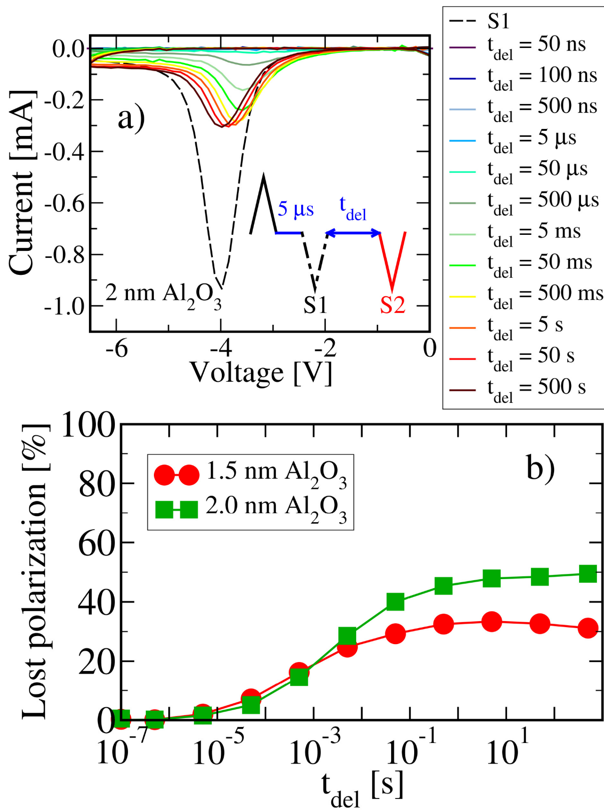


**FIGURE 9. FTJ current-voltage characteristics measured at different delay times after a set operation S1 at T = 300 K (schematic of the measurement waveform in inset), showing $P_r$ loss due to depolarization field and charge detrapping. b) Extracted percentage of remnant polarization lost during $t_{delay}$ observed on a).**

for longer times, with a plateau at typically 30% of the total polarization for an alumina thickness of 1.5 nm. Increasing the alumina thickness from 1.5 nm to 2.0 nm is expected to increase the depolarization field and therefore the polarization loss at a fixed trapped charge areal density, which is in fact observed in Fig. 9.

## V. CONCLUSION

We have shown through a comparison between experiments and simulations that the polarization switching in MFIM based FTJs is greatly influenced by the injection and trapping of charge into the dielectric stack, which compensates the ferroelectric polarization to a large extent. In this paper we have described this behaviour in terms of tunnelling injection through the thin $Al_2O_3$ layer and trapping at the FE-DE interface. However, defects assisted transport through the dielectrics and charge trapping in the HZO film may also contribute to the picture.

We argue that the understanding and control of such a charge compensation is crucial for the design of FTJs based on an MFIM structure. The support of well calibrated simulations can provide a sound basis for the engineering and optimization of this class of electron devices.

## REFERENCES

[1] E. Chicca and G. Indiveri, “A recipe for creating ideal hybrid memristive-CMOS neuromorphic processing systems,” *Appl. Phys. Lett.*, vol. 116, no. 12, 2020, Art. no. 120501. [Online]. Available: https://doi.org/10.1063/1.5142089
[2] S. Yu, “Neuro-inspired computing with emerging nonvolatile memorys,” *Proc. IEEE*, vol. 106, no. 2, pp. 260–285, Feb. 2018.
[3] T. Mikolajick *et al.*, “Next generation ferroelectric memories enabled by hafnium oxide,” in *Proc. IEEE Int. Electron Devices Meeting (IEDM)*, 2019, pp. 1–4.
[4] S. Slesazeck and T. Mikolajick, “Nanoscale resistive switching memory devices: A review,” *Nanotechnology*, vol. 30, no. 35, Jun. 2019, Art. no. 352003. [Online]. Available: https://doi.org/10.1088/1361-6528/ab2084
[5] B. Max, M. Hoffmann, S. Slesazeck, and T. Mikolajick, “Direct correlation of ferroelectric properties and memory characteristics in ferroelectric tunnel junctions,” *IEEE J. Electron Devices Soc.*, vol. 7, pp. 1175–1181, 2019.
[6] R. Fontanini *et al.*, “Polarization switching and interface charges in BEOL compatible ferroelectric tunnel junctions,” in *Proc. IEEE 51st Eur. Solid-State Device Res. Conf. (ESSDERC)*, 2021, pp. 255–258.
[7] E. Covi *et al.*, “Ferroelectric tunneling junctions for edge computing,” in *Proc. IEEE Int. Symp. Circuits Syst. (ISCAS)*, 2021, pp. 1–5.
[8] H. Mulaosmanovic *et al.*, “Impact of read operation on the performance of $HfO_2$-based ferroelectric FETs,” *IEEE Electron Device Lett.*, vol. 41, no. 9, pp. 1420–1423, Sep. 2020.
[9] D. Lizzit and D. Esseni, “Operation and design of ferroelectric FETs for a BEOL compatible device implementation,” in *Proc. IEEE 51st Eur. Solid-State Device Res. Conf. (ESSDERC)*, 2021, pp. 215–218.
[10] A. M. Ionescu and H. Riel, “Tunnel field-effect transistors as energy-efficient electronic switches,” *Nature*, vol. 479, pp. 329–337, Nov. 2011.
[11] D. Esseni, M. Pala, P. Palestri, C. Alper, and T. Rollo, “A review of selected topics in physics based modeling for tunnel field-effect transistors,” *Semicond. Sci. Technol.*, vol. 32, no. 8, 2017, Art. no. 83005. [Online]. Available: http://stacks.iop.org/0268-1242/32/i=8/a=083005
[12] H. W. Park *et al.*, “Polarizing and depolarizing charge injection through a thin dielectric layer in a ferroelectric–dielectric bilayer,” *Nanoscale*, vol. 13, no. 4, pp. 2556–2572, 2021.
[13] K. Toprasertpong, M. Takenaka, and S. Takagi, “Direct observation of interface charge behaviors in FeFET by quasi-static split C-V and hall techniques: Revealing FeFET operation,” in *Proc. IEEE Int. Electron Devices Meeting (IEDM)*, 2019, pp. 1–4.
[14] K. Toprasertpong, Z. Y. Lin, T. E. Lee, M. Takenaka, and S. Takagi, “Asymmetric polarization response of electrons and holes in Si FeFETs: Demonstration of absolute polarization hysteresis loop and inversion hole density over $2\times10^{13}$ $cm^{-2}$,” in *Proc. IEEE Symp. VLSI Technol.*, 2020, pp. 1–2.
[15] J. Li, Y. Qu, M. Si, X. Lyu, and P. D. Ye, “Multi-probe characterization of ferroelectric/dielectric interface by C-V, P-V and conductance methods,” in *Proc. IEEE Symp. VLSI Technol.*, 2020, pp. 1–2.
[16] J. Li, M. Si, Y. Qu, X. Lyu, and P. D. Ye, “Quantitative characterization of ferroelectric/dielectric interface traps by pulse measurements,” *IEEE Trans. Electron Devices*, vol. 68, no. 3, pp. 1214–1220, Mar. 2021.
[17] S. Deng *et al.*, “Examination of the interplay between Polarization switching and charge trapping in ferroelectric FET,” in *Proc. IEEE Int. Electron Devices Meeting (IEDM)*, 2020, pp. 4.4.1–4.4.4.
[18] M. H. Park, H. J. Kim, Y. J. Kim, W. Lee, T. Moon, and C. S. Hwang, “Evolution of phases and ferroelectric properties of thin $Hf_{0.5}Zr_{0.5}O_2$ films according to the thickness and annealing temperature,” *Appl. Phys. Lett.*, vol. 102, no. 24, 2013, Art. no. 242905.
[19] E. D. Grimley *et al.*, “Structural changes underlying field-cycling phenomena in ferroelectric $HfO_2$ thin films,” *Adv. Electron. Mater.*, vol. 2, no. 9, 2016, Art. no. 1600173.
[20] K. M. Rabe, M. Dawber, C. Lichtensteiger, C. Ahn, and J.-M. Triscone, “Modern physics of ferroelectrics: Essential background,” *Physiscs of Ferroelectrics, A Modern Perspective*. Berlin, Germany: Springer, 2007, pp. 1–30, doi: 10.1007/978-3-540-34591-6_1.

[21] M. Fukunaga and Y. Noda, "New technique for measuring ferroelectric and antiferroelectric hysteresis loops," *J. Phys. Soc. Jpn.*, vol. 77, no. 6, 2008, Art no. 64706. [Online]. Available: https://doi.org/10.1143/JPSJ.77.064706

[22] P. D. Lomenzo *et al.*, "Ferroelectric phenomena in Si-doped $HfO_2$ thin films with TiN and ir electrodes," *J. Vac. Sci. Technol. B*, vol. 32, no. 3, p. 3D123, 2014. [Online]. Available: https://doi.org/10.1116/1.4873323

[23] V. Mikheev *et al.*, "Ferroelectric second-order memristor," *ACS Appl. Mater. Interfaces*, vol. 11, no. 35, pp. 32108–32114, 2019. [Online]. Available: https://doi.org/10.1021/acsami.9b08189

[24] H. Ryu, H. Wu, F. Rao, and W. Zhu, "Ferroelectric tunneling junctions based on aluminum oxide/ zirconium-doped hafnium oxide for neuromorphic computing," *Sci. Rep.*, vol. 9, no. 1, Dec. 2019, Art. no. 20383. [Online]. Available: https://doi.org/10.1038/s41598-019-56816-x

[25] V. Deshpande, K. S. Nair, M. Holzer, S. Banerjee, and C. Dubourdieu, "CMOS back-end-of-line compatible ferroelectric tunnel junction devices," *Solid-State Electron.*, vol. 186, Dec. 2021, Art. no. 108054. [Online]. Available: https://www.sciencedirect.com/science/article/pii/S003811012100099X

[26] M. Segatto, R. Fontanini, F. Driussi, D. Lizzit, and D. Esseni, "Limitations to electrical probing of spontaneous polarization in ferroelectric-dielectric heterostructures," *IEEE J. Electron Devices Soc.*, vol. 10, pp. 324–333, 2022.

[27] R. Athle, A. E. O. Persson, A. Irish, H. Menon, R. Timm, and M. Borg, "Effects of TiN top electrode texturing on ferroelectricity in $Hf_{1-x}Zr_xO_2$," *ACS Appl. Mater. Interfaces*, vol. 13, no. 9, pp. 11089–11095, 2021.

[28] T. Rollo, F. Blanchini, G. Giordano, R. Specogna, and D. Esseni, "Revised analysis of negative capacitance in ferroelectric-insulator capacitors: Analytical and numerical results, physical insight, comparison to experiments," in *Proc. IEEE Int. Electron Devices Meeting (IEDM)*, Dec. 2019, pp. 7.2.1–7.2.4.

[29] T. Rollo, F. Blanchini, G. Giordano, R. Specogna, and D. Esseni, "Stabilization of negative capacitance in ferroelectric capacitors with and without a metal interlayer," *Nanoscale*, vol. 12, no. 10, pp. 6121–6129, 2020.

[30] D. Esseni and R. Fontanini, "Macroscopic and microscopic picture of negative capacitance operation in ferroelectric capacitors," *Nanoscale*, vol. 13, no. 21, pp. 9641–9650, 2021.

[31] R. Alcala *et al.*, "Influence of oxygen source on the ferroelectric properties of ALD grown $Hf_{1-x}Zr_xO_2$ films," *J. Phys. D, Appl. Phys.*, vol. 54, no. 3, Oct. 2020, Art. no. 35102. [Online]. Available: https://doi.org/10.1088/1361-6463/abbc98

[32] T. Kim, J. A. del Alamo, and D. A. Antoniadis, "Dynamics of $HfZrO_2$ ferroelectric structures: Experiments and models," in *Proc. IEEE Int. Electron Devices Meeting (IEDM)*, Dec. 2020, pp. 21.4.1–21.4.4.

[33] A. Kerber *et al.*, "Charge trapping and dielectric reliability of $SiO_2$-$al_2O_3$ gate stacks with TiN electrodes," *IEEE Trans. Electron Devices*, vol. 50, no. 5, pp. 1261–1269, May 2003.

[34] Q. Q. Shu and W. G. Ma, "Barrier parameter variation in Al-$Al_2O_3$-metal tunnel junctions," *Appl. Phys. Lett.*, vol. 61, no. 21, pp. 2542–2544, 1992. [Online]. Available: https://doi.org/10.1063/1.108145

[35] Z. Dong, X. Cao, T. Wu, and J. Guo, "Tunneling current in $HfO_2$ and $Hf_{0.5}Zr_{0.5}O_2$-based ferroelectric tunnel junction," *J. Appl. Phys.*, vol. 123, no. 9, 2018, Art. no. 94501. [Online]. Available: https://doi.org/10.1063/1.5016823

[36] N. S. Saks and M. G. Ancona, "Determination of interface trap capture cross sections using three-level charge pumping," *IEEE Electron Device Lett.*, vol. 11, no. 8, pp. 339–341, Aug. 1990.

[37] S. Gupta *et al.*, "Density and capture cross-section of interface traps in $GeSnO_2$ and $GeO_2$ grown on Heteroepitaxial GeSn," *ACS Appl. Mater. Interfaces*, vol. 8, no. 21, pp. 13181–13186, Jun. 2016. [Online]. Available: https://doi.org/10.1021/acsami.6b01582

[38] J. T. Ryan, A. Matsuda, J. P. Campbell, and K. P. Cheung, "Interface-state capture cross section–why does it vary so much?" *Appl. Phys. Lett.*, vol. 106, no. 16, 2015, Art. no. 163503. [Online]. Available: https://doi.org/10.1063/1.4919100

[39] M. Hoffmann *et al.*, "Intrinsic nature of negative capacitance in multidomain $Hf_{0.5}Zr_{0.5}O_2$-based ferroelectric/dielectric heterostructures," *Adv. Funct. Mater.*, vol. 32, no. 2, 2022, Art. no. 2108494. [Online]. Available: https://onlinelibrary.wiley.com/doi/abs/10.1002/adfm.202108494

[40] A. K. Tagantsev and G. Gerra, "Interface-induced phenomena in polarization response of ferroelectric thin films," *J. Appl. Phys.*, vol. 100, no. 5, 2006, Art. no. 51607. [Online]. Available: https://doi.org/10.1063/1.2337009

[41] H. Schroeder, "Poole-Frenkel-effect as dominating current mechanism in thin oxide films—An illusion?" *J. Appl. Phys.*, vol. 117, no. 21, 2015, Art. no. 215103. [Online]. Available: https://doi.org/10.1063/1.4921949

[42] F. Driussi, P. Palestri, and L. Selmi, "Modeling, simulation and design of the vertical graphene base transistor," *Microelectron. Eng.*, vol. 109, pp. 338–341, Sep. 2013. [Online]. Available: https://www.sciencedirect.com/science/article/pii/S0167931713003638

[43] S. Takagi, N. Yasuda, and A. Toriumi, "Experimental evidence of inelastic tunneling in stress-induced leakage current," *IEEE Trans. Electron Devices*, vol. 46, no. 2, pp. 335–341, Feb. 1999.

[44] R. Fontanini, M. Massarotto, R. Specogna, F. Driussi, M. Loghi, and D. Esseni, "Modelling and design of FTJs as high reading-impedance synaptic devices," in *Proc. 5th IEEE Electron Devices Technol. Manuf. Conf. (EDTM)*, 2021, pp. 1–3.